Towards Breaking the Spatial Resolution Barriers: An Optical Flow and Super-Resolution Approach for Sea Ice Motion Estimation

Zisis I. Petrou[a], Yang Xian[b], YingLi Tian[a,b,*]

[a]*Department of Electrical Engineering, The City College of New York, The City University of New York, New York, NY, 10031 USA*
[b]*Department of Computer Science, The Graduate Center, The City University of New York, New York, NY, 10016 USA*

Abstract

Estimation of sea ice motion at fine scales is important for a number of regional and local level applications, including modeling of sea ice distribution, ocean-atmosphere and climate dynamics, as well as safe navigation and sea operations. In this study, we propose an optical flow and super-resolution approach to accurately estimate motion from remote sensing images at a higher spatial resolution than the original data. First, an external example learning-based super-resolution method is applied on the original images to generate higher resolution versions. Then, an optical flow approach is applied on the higher resolution images, identifying sparse correspondences and interpolating them to extract a dense motion vector field with continuous values and subpixel accuracies. Our proposed approach is successfully evaluated on passive microwave, optical, and Synthetic Aperture Radar data, proving ap-

---

*Corresponding author.
Email addresses: `zpetrou@ccny.cuny.edu` (Zisis I. Petrou), `yxian@gradcenter.cuny.edu` (Yang Xian), `ytian@ccny.cuny.edu` (YingLi Tian)

propriate for multi-sensor applications and different spatial resolutions. The approach estimates motion with similar or higher accuracy than the original data, while increasing the spatial resolution of up to eight times. In addition, the adopted optical flow component outperforms a state-of-the-art pattern matching method. Overall, the proposed approach results in accurate motion vectors with unprecedented spatial resolutions of up to 1.5 km for passive microwave data covering the entire Arctic and 20 m for radar data, and proves promising for numerous scientific and operational applications.

1. Introduction

Sea ice motion is a critical factor in climate models and local-level human activities in the polar regions. It significantly affects the thickness distribution of sea ice, causing leads—open water areas—or ridging in cases of divergent or convergent motion, respectively. These dynamic processes coact with thermodynamic ocean-atmosphere processes and affect the ice mass balance and thickness which determine the survival or summer melting of sea ice in a region (Haas, 2017). Convergent motion creates thicker ice and enhances sea ice survival, whereas divergent motion promotes energy and moisture fluxes (Meier, 2017; Gettelman and Rood, 2016). In fact, sea ice motion has been a major factor in the loss of multi-year ice in the Arctic through its advection out of the region (Meier, 2017; Smedsrud et al., 2011). Given these facts, it is an important component for the calculation, initialization, fine-tuning, or validation of climate models that quantify exchanges of

energy and mass between the ocean and the atmosphere and predict polar ice pack conditions (Kræmer et al., 2015; De Silva et al., 2015; Berg et al., 2013; Kimura et al., 2013; Meier et al., 2000). Besides, sea ice motion can significantly affect, or even endanger, human activities on a local level, including ship navigation, fisheries, and oil/gas drilling. Considering the increasing trends on average sea ice drift speed during the last decades (Spreen et al., 2011; Rampal et al., 2009), accurately monitoring sea ice motion at a fine scale is of great importance.

Data from a variety of satellite sensors have been employed to estimate sea ice motion. They include i) passive microwave sensors, e.g., Special Sensor Microwave Imager (SSM/I), Advanced Microwave Scanning Radiometer - Earth Observing System (AMSR-E), Advanced Microwave Scanning Radiometer 2 (AMSR2) (Tschudi et al., 2016b; Girard-Ardhuin and Ezraty, 2012; Lavergne et al., 2010); ii) microwave scatterometers, such as QuikSCAT (Girard-Ardhuin and Ezraty, 2012; Haarpaintner, 2006); iii) Synthetic Aperture Radars (SAR), e.g., ENVISAT Advanced SAR (ASAR), RADARSAT-2, European Remote Sensing 1 (ERS-1) SAR (Karvonen, 2012; Komarov and Barber, 2014; Berg and Eriksson, 2014); and iv) optical, such as Advanced Very High Resolution Radiometer (AVHRR), Moderate Resolution Imaging Spectroradiometer (MODIS) (Ninnis et al., 1986; Emery et al., 1991; Tschudi et al., 2016b; Petrou and Tian, 2017). Although passive microwave and scatterometer sensor data can provide daily coverage of the entire Arctic, their typical spatial resolution of around 5–25 km makes monitoring of small leads and ridges difficult and is prohibitively coarse for any fine-scale applications, such as ship navigation. The resolution of optical data used in sea ice moni-

toring studies can be one order of magnitude higher, between 250 m and 1.1 km. Even in the case of SAR data which have higher resolution of several tens to hundreds of meters, tasks such as estimating motion at a scale of a ship size still remains challenging.

Sea ice motion between two time instances is typically represented through a motion vector field. Each motion vector quantifies the displacement, or velocity, of a sea ice parcel in a pixel or patch in the image from the first to the second time instance. This makes the spatial resolution of sea ice motion described as a two-parameter problem: the first parameter is the *density* of the vector field, i.e., the number of vectors originating from a unit area; the second is the *minimum detectable motion*, i.e., the minimum possible non-zero motion that a vector can describe. Both parameters are restricted by the inherent spatial resolution of the satellite images used. Several sea ice motion estimation approaches have attempted, implicitly or explicitly, to improve one or the other parameter, but rarely both. In addition, most proposed approaches have been evaluated in solely one, or sometimes two, types of sensor data, mainly of similar spatial resolution and nature.

In this study we propose an approach that attempts to accurately estimate sea ice motion, by both increasing the density of the calculated motion field and reducing the minimum detectable motion. An example-based super-resolution technique is explored to increase the inherent resolution of the employed satellite images. Then, an optical flow-based approach is applied to estimate motion in a dense per-pixel field, providing vectors that describe continuous subpixel displacements. In addition, to demonstrate its robustness and transferability in local and regional level studies, the method

is extensively evaluated on passive microwave, optical, and SAR data of different spatial resolutions. To our best knowledge, it is the first sea ice motion methodology applied in satellite data of such high diversity in sensor types and spatial resolutions. In addition, it produces the highest resolution motion vector fields ever generated from each sensor type, reaching up to around 1.5 km for passive and 20 m for SAR data.

This paper is organized as follows. Previous work related to sea ice motion and super-resolution is presented in Section 2. Section 3 details the data employed in this study and Section 4 describes the proposed methodology. Experimental results and discussions on the outcomes are presented in Sections 5 and 6, respectively. Main conclusions are drawn in Section 7.

2. Related work

The vast majority of sea ice motion estimation studies have been based on pattern matching—or *template* matching—approaches. Given a template on an image, i.e., an image patch, these approaches search for the candidate template in a second image, captured later in time, with the most similar pattern to the first one. Based on the relative distance and orientation of the two templates, the motion of the patch—and of the underlying sea ice parcel—during the time interval between the two images can be estimated. The motion has been expressed either as displacement or as mean velocity, by dividing the displacement with the time interval.

Normalized cross-correlation (NCC) has been a pattern similarity measure widely employed to be maximized by several studies with satellite data (Ninnis et al., 1986; Emery et al., 1991; Kwok et al., 1998; Meier et al.,

5

2000; Meier and Dai, 2006; Haarpaintner, 2006; Lavergne et al., 2010; Girard-Ardhuin and Ezraty, 2012; Tschudi et al., 2010, 2016b), and airborne data (Hagen et al., 2014). For a template A centered in position $p = (x, y)$ in one image and a template B centered in position $p + \boldsymbol{u} = (x + u_x, y + u_y)$ in a second image, NCC is calculated as $NCC(\boldsymbol{u}) = cov(A, B)/[\sigma(A)\sigma(B)]$ (Gao and Lythe, 1996), where $cov(A, B)$ stands for the covariance between A and B, $\sigma(A)$ and $\sigma(B)$ for the standard deviations of the pixel values of A and B, respectively, and $\boldsymbol{u} = (u_x, u_y)$ for the motion vector. More recent approaches employed Phase Correlation (PC) as a pattern similarity measure alternative to (Karvonen, 2012; Berg and Eriksson, 2014) or in combination with NCC (Thomas et al., 2008, 2011; Hollands and Dierking, 2011; Komarov and Barber, 2014), to counterbalance the inherent shortcoming of NCC in rotational motion. For templates A and B, PC is calculated in the Fourier domain as their normalized cross-power spectrum and transformed back to the spatial domain as $PC = \mathcal{F}^{-1}(F_A^* F_B / |F_A^* F_B|)$ (Berg and Eriksson, 2014; Karvonen, 2012), where F_A^* represents the conjugate Fourier transform of A, F_B is the Fourier transform of B, and $\mathcal{F}^{-1}$ is the inverse Fourier transform operator. PC is expressed as a matrix in the spatial domain, with the relative motion of the templates estimated from the location corresponding to the maximum value of the PC matrix. In their conceptual form, both NCC and PC approaches are able to express displacements at least equal, or larger, than one pixel of the image. Thus, the estimated motion in each of the two Euclidean axes is quantized to the pixel resolution.

A number of studies attempted to provide subpixel motion estimation through modifications of the original pattern matching approaches. Linear

6

oversampling by a factor of four has been applied in the vector field in order to approximate displacements four times smaller than the original maximum cross-correlation algorithm (Tschudi et al., 2016b; Meier and Dai, 2006; Meier and Maslanik, 2003; Meier et al., 2000). Oversampling on the image data by a factor of six was applied by Kwok et al. (1998) to provide subpixel motion estimation, followed by a biquadratic surface fitting in the correlation value domain. Lavergne et al. (2010) expressed the search for a matching template as a continuous maximization problem, with subpixel motions being estimated using bilinear interpolation. Despite the attempts to decrease the motion quantization error, none of the studies explicitly attempted to increase the density of the motion vector field.

Optical flow has been an alternative approach to pattern matching for sea ice motion estimation. The approach is mainly based on the *brightness constancy* assumption that the intensity of a pixel remains the same during its motion between two images (Fleet and Weiss, 2006). The relative displacement of each pixel between the images is calculated, thus, optical flow approaches result in a dense motion vector field. They usually involve a variational minimization process which results in motion vectors estimated in the continuous domain. Although some early studies on sea ice motion estimation employed optical flow (Sun, 1996; Leppäranta et al., 1998; Gutiérrez and Long, 2003), pattern matching remained the most popular choice. In a recent study, an optical flow method applied to MODIS imagery outperformed a state-of-the-art pattern matching approach in both accuracy and processing speed (Petrou and Tian, 2017). Despite the fact that optical flow approaches provide dense motion vector fields, none has attempted to im-

7

prove this density beyond the boundaries imposed by the image resolution.

Example-based image super-resolution has been popular in recent studies. Different from other approaches where the prior or model is learned in a parametric form regularizing the whole image, this group of methods utilizes the dependencies of small exemplar patches across scales to upscale the low-resolution instances. Learning of the dependencies can be performed via an external dataset (Dong et al., 2015; Kim et al., 2016), within the input image only (Huang et al., 2015; Xian and Tian, 2016), or from combined resources (Yang et al., 2013; Xian et al., 2015). Image super-resolution manages to enhance the image quality for further analysis in a variety of applications such as medical imaging, video surveillance, and remote sensing. A super-resolution variable-pixel linear reconstruction method was described by Merino and Núñez (2007) to obtain high spatial resolution satellite images utilizing multiple lower resolution input images. Ardila et al. (2011) presented a probabilistic method using Markov random field based super-resolution mapping to detect tree crowns in urban areas from remote sensing datasets. In Li et al. (2014), a spatial-temporal Hopfield neural network based super-resolution mapping was proposed to produce land cover maps with a finer spatial resolution than the remotely sensed images. Super-resolution has been recently effectively applied on reconstructing downsampled passive microwave and infrared images for motion estimation and tracking of sea ice floes (Xian et al., 2017).

3. Data

The proposed optical flow with super-resolution approach is evaluated on datasets from sensors of different nature and spatial resolutions. The extent of the AMSR2 data and the regions enclosing the selected areas are drawn in Fig. 1. The precise coordinates of each study area are described in the Supplementary Material. To encourage reproduction of or comparison with our results, all data employed in this study will be publicly released. In particular, these data include all original and super-resolved satellite images, i.e., the finer-scale images generated by the super-resolution algorithm, as well as the validation data described in Section 5.2.

3.1. AMSR2

Passive microwave AMSR2 data are provided by the JAXA Earth Observation Research Center[1]. The data offer daily coverage of the entire Arctic, being insensitive to weather or sun illumination conditions. In particular, daily averaging level 2 brightness temperature swath data of horizontal polarization at 36.5 GHz are employed. The daily images range from January 1–7, 2013, i.e., six pairs in total, and cover the entire Arctic. The data are gridded on a 12.5 km polar stereographic grid tangent to the Earth's surface at 70 degrees northern latitude (NSIDC, 2016). The size of these images is 608×896 pixels, i.e., covering an area of approximately 85 million km^2.

---

[1]http://suzaku.eorc.jaxa.jp/GCOM_W/data/data_w_dpss.html

Figure 1: The entire depicted area represents the extent of the AMSR2 data used in the study. The solid-line rectangle regions, MOD1 and MOD2, enclose the two selected areas covered with MODIS images. The SEN1 dashed-line ellipse encloses two out of the total nine selected areas covered with Sentinel-1 data, whereas SEN2 encloses the rest seven areas. All data are projected on a polar stereographic grid (NSIDC, 2016).

3.2. MODIS

MODIS data have only been used recently in sea ice motion estimation (Petrou and Tian, 2017), mainly due to the restricted availability under lack of sun illumination (polar winter) and cloud contamination in the atmosphere. In this study, MODIS images from two non-overlapping areas nearby the Beaufort Sea (Fig. 1, regions MOD1 and MOD2) are employed, from the period between March 4 and April 20, 2014. Based on the outcomes by Petrou and Tian (2017), level 2G atmospherically corrected images from the Terra satellite gridded into a sinusoidal map projection are used, i.e., the MOD09GQ surface reflectance product (Vermote and Wolfe, 2015). In particular, data from the near-infrared band 2 (841–876 nm), with a spatial resolution of 231.66 m, are used. The data are reprojected to a polar stereographic grid (NSIDC, 2016), using nearest-neighbor interpolation to preserve intensity values and minimize any edge-smoothing effects. To reduce cloud affected pixels, that appear brighter, a 3×3 pixel medium filter and a 5×5 pixel minimum filter are applied. Overall, a set of 23 images with minimal cloud contamination are selected, organized in 12 pairs with one-day interval. The sizes of the images of the two areas are 360×360 and 512×360 pixels, covering areas of approximately 6955 km^2 and 9891 km^2, respectively.

3.3. Sentinel-1

In addition to the coarse resolution passive microwave and medium resolution optical data, high resolution SAR data from Sentinel-1 are also employed to evaluate the proposed approach under different datasets. Sentinel-1A data from nine areas, with some overlaps, are selected, from different parts of the Arctic region (Fig. 1, two areas enclosed within region SEN1 and seven areas

11

withing region SEN2) between January 1 and May 31, 2015. Level-1 Ground Range Detected products with horizontal-horizontal (HH) polarization from the Extra Wide Swath (EW) sensor mode are retrieved from the Copernicus Open Access Hub[2]. To enhance consistent detection of sea ice edge characteristics, only ascending orbit images are selected. The images are radiometrically calibrated, speckle filtered with a 7×7 pixel window Lee Sigma filter (Lee and Pottier, 2009), and orthorectified using Average Height Range Doppler Ellipsoid (Small and Schubert, 2008). Similarly to the previous products, the images are reprojected to a polar stereographic grid (NSIDC, 2016), using nearest-neighbor interpolation. The calibrated sigma values are then converted to dB. The spatial resolution of the original images is 40 m per pixel. However, in order to monitor sea ice motion among sequences of images, the size of the images would be significantly large, and would get even larger after the super-resolution upsampling is applied. For computational purposes, we do not directly apply super-resolution to the original images of 40 m spatial resolution, but first downsample them to generate images of 160 m resolution using Lanczos filtering. We use the latter images as the primary SAR data in our approach, i.e., we apply the super-resolution algorithm on the images of 160 m spatial resolution. Most of these images have a size of 360×360 pixels, covering an extent of around 3318 km^2. Overall, 75 images organized in 66 pairs are selected, with intervals ranging from one to five days.

---

[2]https://scihub.copernicus.eu/

12

3.4. Additional data

In order to train the super-resolution model described in Section 4.1, a set of 6152 natural images (non-satellite images) are used. The images are collected from the Berkeley segmentation (Martin et al., 2001) and LabelMe (Russell et al., 2008) datasets, including a variety of natural images with different objects and scenes.

4. Methods

Fig. 2 draws the flowchart of the proposed approach, which consists of two main components. The super-resolution component creates higher resolution images that serve as input to the optical flow component, which calculates the motion vectors between each image pair.

4.1. Super-resolution

In our framework as illustrated in Fig. 2, we adopt an external example learning-based super-resolution approach presented by Xian et al. (2015), which relies on learning multiple regression models from an external image dataset to ensure a stable super-resolution performance. Different from the hybrid attempt in Xian et al. (2015, 2017), the self-awareness step is not performed in the proposed system. It is based on the observation that since large scaling factors are needed in the aforementioned applications, the gradient level self-awareness step takes relatively longer time as the scaling factor gets larger and additional reconstruction process is needed. Besides, contrary to ordinary super-resolution applications where performance is evaluated based
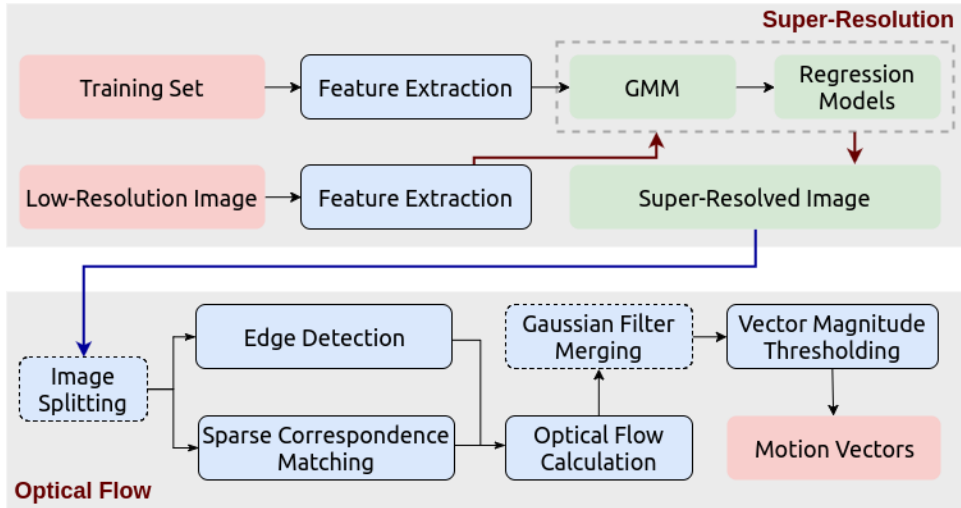
13

Figure 2: Flowchart of the proposed optical flow with super-resolution approach. Input and output data are shown in pink blocks, intermediate results in green, mandatory processing steps in blue with solid-line border and optional steps, depending on processing requirements, in blue blocks with dashed-line border.

on signal-to-noise ratio measures or how visually pleasing the generated images are, in this application performance is based on the accuracy of the motion vectors. Experimental results indicate that skipping the self-awareness step provides similar or more accurate vectors overall for the variety of sensor data than including it. Therefore, we adopt an external example-based approach to ensure the efficiency and maximize the practicality.

A group of pre-trained regression models is firstly generated utilizing a large external image dataset. The input feature space is modeled with Gaussian Mixture Models (GMM) to ensure a targeted and effective learning. GMM is selected since it is a generative model with the capacity to model any given probability distribution function when the number of the Gaussian components is large enough. During the offline training, low-resolution/high-

14

resolution patch pairs in the training dataset are associated with the corresponding Gaussian component, and later within each Gaussian component a regression model is trained and saved. During the online super-resolution, each low-resolution patch in the input image is assigned to a Gaussian component according to the posterior where the corresponding regression model is applied to obtain the high-resolution patch. Simple averaging is adopted to blend overlapping pixels to generate the final high-resolution output.

4.2. Optical flow

An optical flow approach is employed to estimate sea ice motion between each image pair. The approach is based on the methodology implemented by Petrou and Tian (2017), that has shown advantageous properties over a state-of-the-art pattern matching approach using MODIS images. Motion is calculated on a dense field, i.e., for each pixel of the images. This means that for each upscaled version of the images generated by the super-resolution approach, the same increase in the density of the calculated motion vector is achieved.

The motion estimation approach begins with the detection of edges in the first image of an image pair. Edges mainly represent the boundaries between neighboring ice floes, and indicate areas, i.e., ice parcels, where motion can be considered rigid. The edges are detected following a structured learning approach (Dollár and Zitnick, 2015). The image is split into patches and random forests are employed to assign structured labels, i.e., local edge masks, to each patch. The patch level masks are then aggregated and form the final edge mask of the image, in a computationally efficient manner. Independently to the edge detection process, the image pair is employed to detect

15

sparse correspondences. This step is applied to detect distinct matching features in the two images that will facilitate the flow estimation at a later step of the process. The correspondences are calculated following a multi-stage approach (Weinzaepfel et al., 2013). The first image of the pair is split into small non-overlapping patches and the Scale Invariant Feature Transform (SIFT) descriptor (Szeliski, 2011) is calculated. Each patch is split into four quadrants and their best matching correspondences in the second image are detected. The process is repeated increasing at each step the dimensions of the patches by a factor of two and using the information from the previous step. This hierarchical approach discourages locally inconsistent matching, which allows at the same time discovery of matches that correspond to inhomogeneous motion or non-rigid transformations, e.g., creation of leads and ridges, in ice floes. Finally, a number of sparse correspondences with a high density are detected. Additionally to Petrou and Tian (2017), an upper distance threshold to look for a matching correspondence is applied in this study, that considerably speeds up the detection process without sacrificing the accuracy. The threshold is selected to be 2.5 times the theoretical maximum daily motion for sea ice of 60.48 km, as adopted in previous studies (Tschudi et al., 2016b). This threshold is small enough to restrict the search for matching correspondences to only the possible motion range that significantly speeds up the process, and large enough to safely capture even the maximum motions.

The outcomes of the edge detection and sparse correspondence estimation steps are used as inputs to calculate the optical flow. Sparse-to-dense interpolation is performed on the image pair to estimate correspondences for every

16

pixel. Each pixel, p, of the first image that does not belong to the sparse correspondences detected in the previous step is assigned to its closest pixel, p_c, in the sparse correspondence set, C, based on a geodesic distance. The geodesic distance is calculated as the minimum distance among all paths between p and p_c, penalizing the paths that involve crossing the edges detected at the first step, as described in Eq. 3 in Revaud et al. (2015). For each pixel, p, on the first image, its nearest neighbors, $p_c \in C$, are identified, together with their matching pixels, p'_c, in the second image. The matching pixel of p in the second image, p', is found as a locally-weighted affine transformation $p' = A_p p + t_p$, where A_p and t_p are the affine transformation parameters for p. The parameters are estimated by forming a least-square system of equations using the matching correspondences of the closest neighbors of p in C. Based on the solution of the system, the correspondences of all pixels $p \notin C$ on the first image are detected on the second one. Then, variational energy minimization is performed on the resulting dense correspondences to calculate the final optical flow for the image pair (Revaud et al., 2015).

An additional processing step is introduced to account for cases of super-resolved image pairs, mainly by four or eight times, where the optical flow cannot be directly calculated because of computational memory constraints. In such cases, the images are split into 9 (3×3) or 49 (7×7) overlapping subimages and the optical flow is calculated for each subimage separately. Two side-by-side subimages overlap by half their size, e.g., when splitting an original image of size $W \times H$ into nine subimages (three at each direction), the size of the subimages is $W/2 \times H/2$, and the overlapping area between two side-by-side subimages is $W/4 \times H/2$ for the horizontal direction ($W/2 \times H/4$

17

for the vertical direction). The rationale behind overlapping subimages is to attenuate discontinuities near the edges of a subimage after merging the individually calculated optical flow subimages to a single flow image of the original size. The subimages are weighted element-wise with 2D rotationally symmetric Gaussian lowpass filter with the same size as the subimage. Thus, in the merging process, the optical flow value of a pixel where two or more subimages overlap is calculated as the normalized weighted sum of the corresponding overlapping pixels, where each pixel is weighted inversely proportionally to its distance from the center of the subimage it belongs to. This favors optical flow values calculated near the center of the corresponding subimage and assigns less confidence to the values close to the edges. Thus, this approach encourages the calculation of a smooth and consistent optical flow field after merging the individual subimages, and attenuates discontinuities in the subimage edges. After experimentation, the standard deviation of the Gaussian filters is set equal to $minimum(w, h)/8$, where w and h stand for the width and height of the subimages in pixels, respectively.

Finally, same as in previous studies (Petrou and Tian, 2017; Tschudi et al., 2016b), a maximum daily motion threshold is applied. In particular, any optical flow vectors exceeding a magnitude equivalent to 60.48 km/day, are cropped to 60.48 km.

5. Results

5.1. Comparison with pattern matching

The proposed optical flow approach is compared against a state-of-the-art pattern matching approach, described by Petrou and Tian (2017), and noted

18

361 hereafter as "MCC" (Maximum Cross-Correlation) approach. MCC is based
362 on a multi-resolution hierarchical approach (Thomas et al., 2011; Hollands
363 and Dierking, 2011) involving both NCC and PC as similarity measures to
364 estimate motion between images.

5.2. Validation strategy

366 The motion vectors calculated by the optical flow and MCC approaches
367 are evaluated against buoys from the International Arctic Buoy Programme
368 (IABP) (Tschudi et al., 2016a). Their estimated position accuracy is ap-
369 proximately 0.5 km/day (Meier and Dai, 2006; Tschudi et al., 2016a). Buoy
370 positions are reported every 12 hours. In this study, the reported positions
371 at 12:00 GMT are used to estimate the ground-truth daily motion. Due
372 to the limited number of buoys, especially for the Sentinel-1 images which
373 may have only one buoy for reference, the motion vectors from the National
374 Snow and Ice Data Center (NSIDC) gridded Polar Pathfinder daily 25 km
375 EASE-Grid (Equal-Area Scalable Earth Grid) version 3 product (Tschudi
376 et al., 2016b) are additionally used to evaluate the proposed motion esti-
377 mation approach. The vectors are produced using information from buoys,
378 AVHRR, and passive microwave data. Their spatial resolution of 25 km is
379 significantly coarser than the estimated motion and the reported accuracy
380 lies in 3.29–5.24 cm/sec (Tschudi et al., 2016b), i.e., around 3–4 km/day.
381 However, the product is employed here as an additional source of evaluating
382 mainly the consistency in the direction of the estimated vectors. Besides,
383 the availability of a larger number of vectors than the IABP buoys further
384 enhance the statistical analysis. Both the IABP and Polar Pathfinder vectors
385 are reprojected to the adopted polar stereographic grid (NSIDC, 2016).

19

For consistency of the optical flow and MCC evaluation, the optical flow vectors in the same position as the MCC motion vectors are considered. Following the commonly adopted approaches (Meier and Dai, 2006; Lavergne et al., 2010), and in order to avoid interpolating neighboring MCC motion vectors that would require potentially erroneous distribution assumptions, the closest motion vector to each buoy or grid motion vector is employed for the evaluation. It is noted that all evaluations are performed based on the drift, or displacement, rather than motion velocity. Average velocity vectors for each image pair can be extracted through a simple division of these displacements by the time interval between the image pair.

5.3. AMSR2 motion vectors

The AMSR2 images are upscaled by two, four, and eight times using the proposed super-resolution approach, resulting in 6.25 km, 3.125 km, and 1.5625 km resolution images, respectively. Optical flow and MCC are calculated for each of the six image pairs in each resolution and compared against the ground-truth buoy and grid vector data.

Table 1 presents the average performance of the different resolution and method pairs under various evaluation measures, in particular mean-absolute error (MAE), root mean-squared error (RMSE), relative squared error (RSE), and Pearson correlation coefficient (P), for both the horizontal and vertical motion directions. The proposed optical flow approach with the super-resolved images by two (X2) and four (X4) times provides more accurate results than the optical flow applied in the original images. That is, besides the increase of the density of the motion vector field by 4 (2×2 for the two directions of the X2 images) and 16 (4×4) times, increase in the accuracy of

20

the detected motion is additionally achieved. Even further, comparing MCC results on the original and X8 images, it appears that super-resolution leads to both more accurate results and an increase in vector field density by 64 times (8×8). Optical flow outperforms MCC for the original as well as the X2 and X4 super-resolved images. The optical flow on the X8 super-resolved images is calculated separately in the overlapping subimages of an image and then merged together (Section 4.2). For these images MCC provides more accurate results. Moreover, all super-resolved images under both optical flow and MCC provide more accurate results compared with the current state of the art, i.e., the application of MCC on the original images. The results are consistent among the different evaluation measures employed, further supporting these observations.

Fig. 3 offers a close look on the calculated motion vectors on the central Arctic region for a X2 super-resolved indicative image pair. The optical flow vectors (Fig. 3a) appear to correlate significantly better with the reference buoy vectors than the MCC ones (Fig. 3b), both in the motion direction and magnitude. This can be observed more clearly on the left part of the images, where the MCC motion vector field has several changes in magnitude and direction within the same and across the spatial resolution images, whereas the flow vectors appear more consistent. The results are similar for the original as well as the X4 and X8 super-resolved images which are drawn in the Supplementary Material.

In the aforementioned results, the MCC vector nearest to each buoy is used for the evaluation, since MCC vectors are not calculated for each pixel. For a fair comparison, the optical flow vectors on the same position in the

21

Table 1: Accuracy evaluation of the optical flow ("Flow") and pattern matching ("MCC") vectors, for all six image pairs of AMSR2 data, against IABP buoys, 122 vectors for the overall period. Super-resolved images by two, four, and eight times are indicated as "X2," "X4," and "X8," respectively. Evaluations are performed on both the vertical ("δx") and horizontal ("δy") axes, through mean-absolute error in km (MAE), root mean-squared error in km (RMSE), relative squared error (RSE), and the Pearson correlation coefficient (P). For MAE, RMSE, and RSE the smaller numbers indicate more accurate results, while the opposite holds for P. The best results for each measure are highlighted in bold.

	δx				δy			
	MAE	RMSE	RSE	P	MAE	RMSE	RSE	P
Flow	1.944	3.090	0.387	0.803	1.917	2.728	0.110	0.944
Flow-X2	**1.487**	**2.524**	**0.258**	**0.883**	1.382	2.103	0.065	0.967
Flow-X4	1.720	3.204	0.416	0.812	**1.284**	**2.000**	**0.059**	**0.970**
Flow-X8	2.651	4.696	0.893	0.481	3.198	5.156	0.393	0.792
MCC	3.571	5.234	1.110	0.490	4.724	7.054	0.735	0.702
MCC-X2	2.836	4.270	0.739	0.628	2.880	4.528	0.303	0.856
MCC-X4	2.209	3.886	0.612	0.676	2.176	3.163	0.148	0.927
MCC-X8	2.560	4.185	0.710	0.627	3.060	4.642	0.318	0.843

image with the selected MCC vectors are employed. It is noteworthy, though, that evaluating the optical flow vectors on the exact position of the buoys, instead, can slightly further decrease the estimation errors, as shown in Fig. 4.

The evaluation against the 25-km NSIDC grid vectors (overall 127,428 vectors for the entire six-pair image set) provides in general consistent indications with the buoys. A subset of the results is shown in Table 2, with the
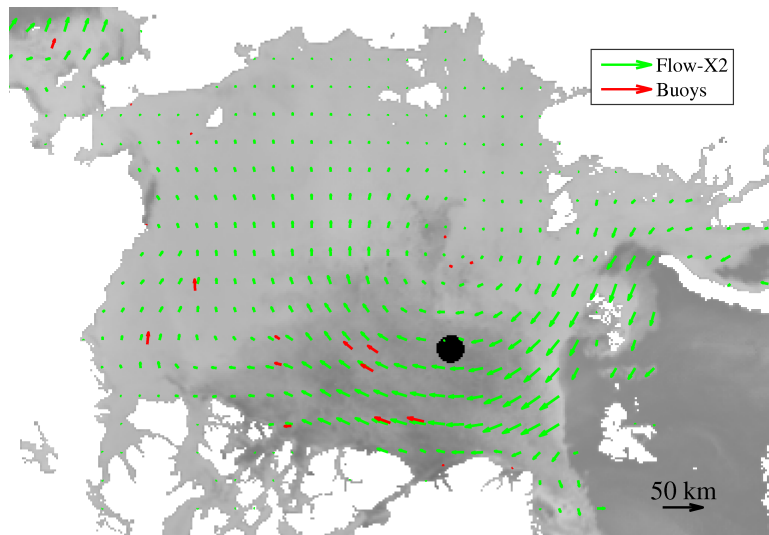
(a)
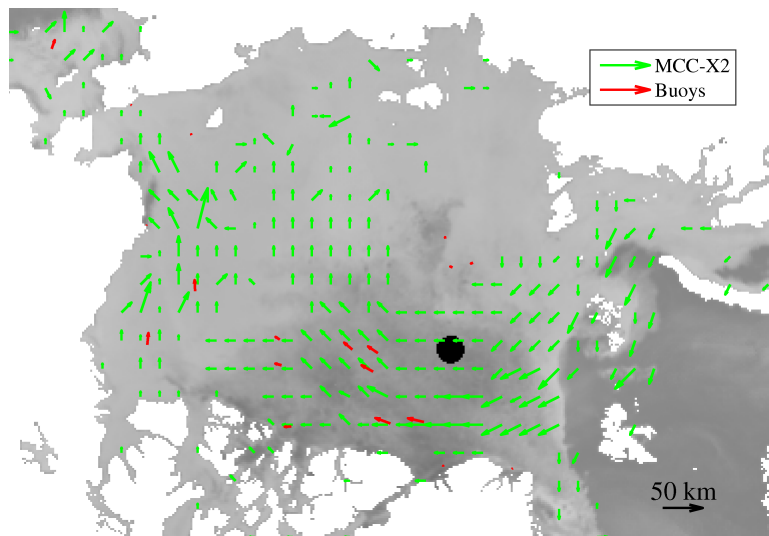
(b)

Figure 3: Close-up look of the calculated motion vectors on the super-resolved AMSR2 images by a factor of two from Jan. 2 to Jan. 3, 2013. For better illustration, only subset of the vectors are drawn. (a) Optical flow vectors. (b) MCC vectors.
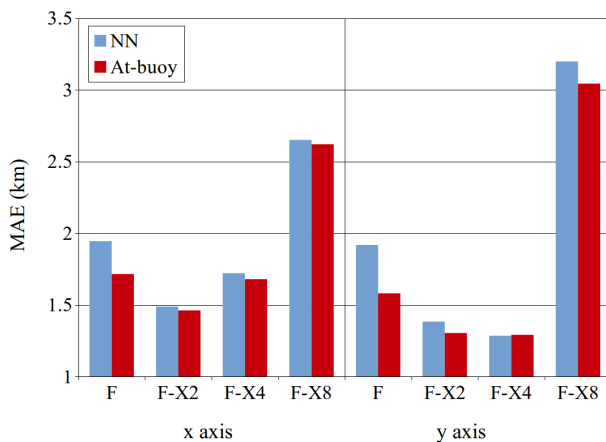
Figure 4: MAE of optical flow vectors for AMSR2 of the entire period (122 buoy vectors), when the optical flow vectors on the exact position of each buoy ("At-buoy") and the ones at the position of the MCC vector nearest to the respective buoy ("NN") are used for evaluation. "F-Xi" stands for optical flow on the super-resolved images by a factor of i.

rest shown in the Supplementary Material. Optical flow consistently outperforms MCC in all image resolutions, with MCC in the original image set providing the least accurate results. Optical flow calculated on the original image resolution appears slightly more accurate than the super-resolved versions in this case. However, the super-resolved images still lead to increased density in the calculated vector field compared with the original images by up to 64 times (in upscaling by eight in the two dimensions) without significantly sacrificing accuracy. It can be observed that some fine scale motions captured in the super-resolved images might not be appropriately expressed by the coarser 25-km resolution grid vectors.

Table 2: Accuracy evaluation of the optical flow and MCC vectors for AMSR2 data against 25-km NSIDC grid vectors, 127,428 vectors for the overall period. MAE in km is shown for the vertical ("MAE-x") and horizontal ("MAE-y") axes.

	MAE-x	MAE-y
Flow	**1.970**	**2.240**
Flow-X2	2.090	2.389
Flow-X4	2.425	2.475
Flow-X8	2.737	2.484
MCC	4.656	5.698
MCC-X2	3.794	4.115
MCC-X4	3.815	4.081
MCC-X8	4.403	4.579

5.4. MODIS motion vectors

Similar to the AMSR2 data, the MODIS original resolution images are super-resolved by a factor of two, four, and eight, resulting in images with 115.83 m, 57.92 m, and 28.96 m spatial resolution, respectively.

Table 3 presents the evaluation accuracy results on the 12 image pairs compared with the IABP buoys (81 buoy vectors in total). Vectors calculated with the original images are more accurate than the super-resolved sets both for the optical flow and MCC methods. However, the performance with the super-resolved images remains similarly high, especially for the X2 and X4 versions, increasing the density of the motion vector field without significantly sacrificing accuracy. As far as the estimation methodologies are concerned, optical flow consistently outperforms MCC for all image versions, apart from the motion on the vertical axis captured with the X8 images.

25

Table 3: Accuracy evaluation of the optical flow and MCC vectors, for all 12 image pairs of MODIS data, against IABP buoys, 81 vectors for the overall period. MAE and RMSE errors are in km.

	δx				δy			
	MAE	RMSE	RSE	P	MAE	RMSE	RSE	P
Flow	**1.092**	**1.811**	**0.262**	**0.860**	**0.942**	1.383	0.445	**0.850**
Flow-X2	1.136	1.823	0.265	0.859	0.983	**1.369**	**0.436**	0.833
Flow-X4	1.313	2.104	0.354	0.809	1.330	2.360	1.295	0.670
Flow-X8	3.044	4.197	1.407	0.395	1.582	2.084	1.010	0.518
MCC	1.242	1.984	0.314	0.836	1.091	1.579	0.580	0.812
MCC-X2	1.303	1.975	0.312	0.833	1.417	2.044	0.972	0.708
MCC-X4	1.572	2.228	0.396	0.786	1.606	2.244	1.171	0.664
MCC-X8	1.773	2.620	0.548	0.700	2.058	3.117	2.259	0.562

Fig. 5 illustrates an indicative example of the calculated motion vectors for the second area of MODIS images (area M2, see Supplementary Material, enclosed within region MOD2 in Fig. 1) and the image pair of March 28 and 29, 2014. In line with the quantitative results, the optical flow vectors are more consistent than the MCC ones, especially on the right part of the image. On the same part of the image, some optical flow vectors from the X8 image with incorrect direction or underestimated magnitude can also be observed. On the largest part of the area, though, including the limited area where buoys fall, the resulting vectors are similar for the original and the super-resolved versions, for both the optical flow and MCC methods, indicating that no significant loss in accuracy is observed for even the X8

26

super-resolved images.

Comparison with the 25-km resolution NSIDC grid data provides overall consistent results. In fact, under this evaluation dataset, optical flow vectors in the X2 super-resolved images provide the best overall results, outperforming even the optical flow on the original images, under almost all accuracy evaluation measures (Table 4). The grid vectors are almost double in number than the buoy ones, and are spread more uniformly in the area (on a 25-km orthogonal grid) contrary to the buoys whose positions follow more randomized patterns (e.g., Fig. 5). Thus, they apply different spatial sampling and contribute complementary information to the statistical errors measured with the buoys. The evaluation with the grid data further supports the advantages brought by the super-resolution approach. It is also noteworthy that the MAE and RMSE errors are overall larger in grid data than with buoys (Table 3), due to the coarse resolution of the former that heavily quantizes motion that can be captured in more detail by the buoys and the MODIS images.

5.5. Sentinel-1 motion vectors

As previously, super-resolved versions of the Sentinel-1 images by a factor of two, four, and eight are created. These result in images with 80 m, 40 m, and 20 m spatial resolution, respectively.

The calculated motion vectors are first evaluated against the IABP buoys (Table 5). For each specific spatial resolution, the calculated motion vectors with optical flow and MCC appear to have similar accuracies, with the latter slightly outperforming the former. The overall best results are achieved when MCC is applied on the super-resolved images by a factor of two. In fact, the
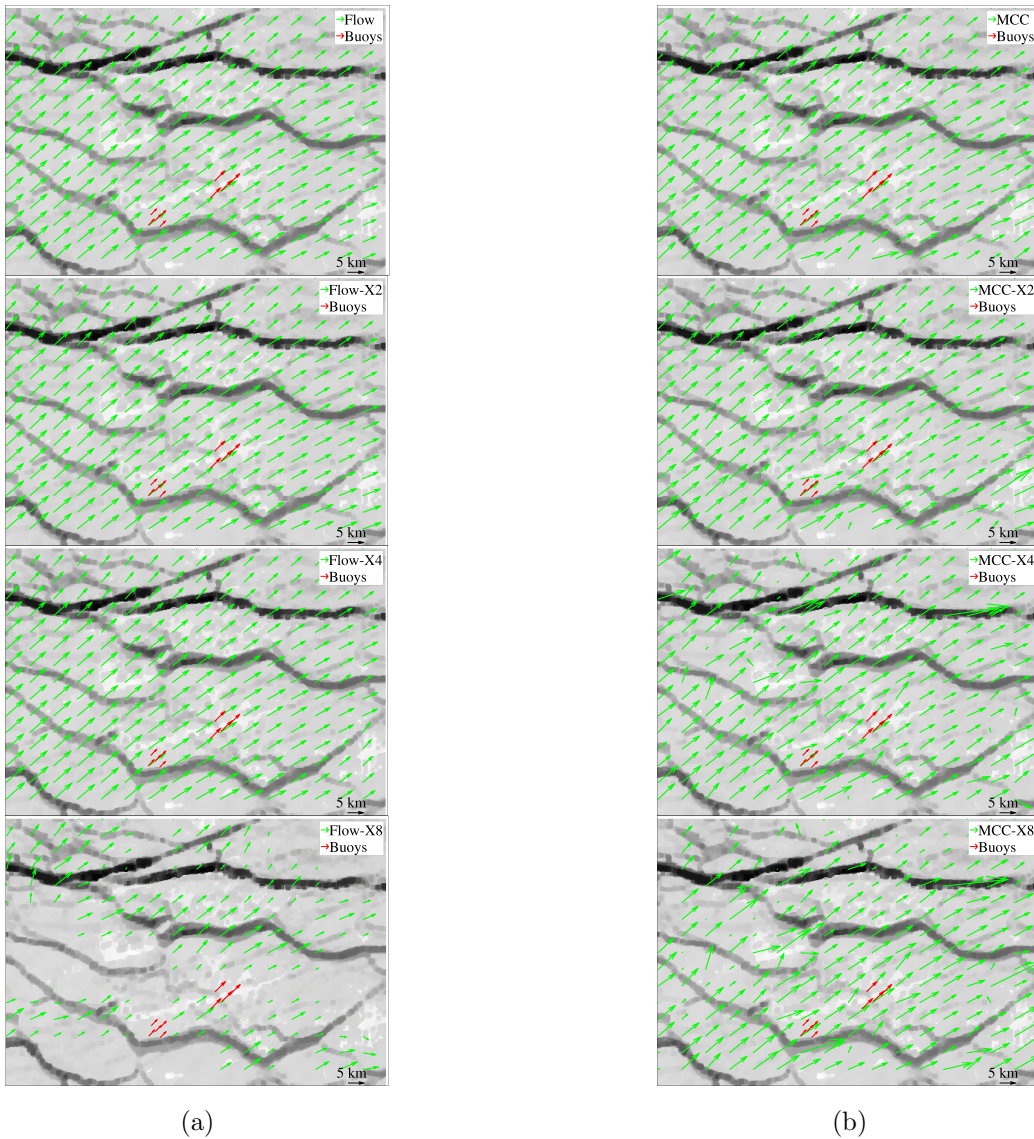
27

(a)   (b)

Figure 5: Calculated motion vectors on the original and super-resolved MODIS images for the second of the two areas from Mar. 28 to Mar. 29, 2014. For better illustration, only subset of the vectors are drawn. (a) From top to bottom, optical flow vectors from the original and super-resolved images by a factor of two, four, and eight. (b) The respective MCC vectors.

Table 4: Accuracy evaluation of the optical flow original and X2 super-resolved image vectors, for all six image pairs of MODIS data, against NSIDC grid vectors, 150 vectors for the overall period. MAE and RMSE errors are in km.

		Flow	Flow-X2
δx	MAE	1.292	**1.279**
	RMSE	1.798	**1.768**
	RSE	0.270	**0.261**
	P	0.856	**0.862**
δy	MAE	**1.137**	1.151
	RMSE	1.649	**1.642**
	RSE	0.792	**0.785**
	P	0.880	**0.894**

super-resolved X2 images provide better results than the original images for both optical flow and MCC, whereas the X4 images provide similar results. This demonstrates the fact that, besides the increase on the density of the motion vector field of even up to 16 times (4×4), insignificant loss or even an increase in accuracy is also achieved by the proposed super-resolution approach.

Due to the high resolution of the Sentinel-1 images, the covered area is smaller than the MODIS images, and significantly smaller than the AMSR2 images. This results in having only one or two buoy vectors present on each image, 75 in total. In order to artificially double the number of statistical samples, we additionally consider the horizontal and vertical components of the vectors as individual vectors, as has been applied in sea-ice motion studies with limited number of vectors (Hollands and Dierking, 2011).

Table 5: Accuracy evaluation of the optical flow and MCC vectors, for all 66 image pairs of Sentinel-1 data, against IABP buoys, 75 vectors for the overall period.

	δx				δy			
	MAE	RMSE	RSE	P	MAE	RMSE	RSE	P
Flow	0.378	0.599	0.050	0.976	0.437	1.047	0.124	0.971
Flow-X2	0.362	0.590	0.049	0.977	0.435	1.017	0.117	0.972
Flow-X4	0.368	0.637	0.057	0.972	0.742	2.340	0.622	0.651
Flow-X8	0.653	1.746	0.427	0.761	0.732	2.040	0.472	0.750
MCC	0.339	0.476	0.032	0.985	0.432	0.927	0.097	0.977
MCC-X2	**0.312**	**0.449**	**0.028**	**0.987**	**0.354**	**0.620**	**0.044**	**0.987**
MCC-X4	0.360	0.694	0.068	0.974	0.439	1.009	0.116	0.948
MCC-X8	0.420	0.813	0.093	0.966	0.503	1.072	0.130	0.943

Two-sample Kolmogorov-Smirnov test confirms—does not reject—the null-hypothesis that the horizontal and vertical components come from the same distribution at the 5% significance level. Analysis of the 150 vectors together provides consistent results with the ones reported in Table 5.

Evaluating the calculated vectors against the NSIDC grid data (311 vectors overall), optical flow on the original resolution images provides the best overall accuracy. This is an indication that the proposed optical flow and MCC vectors perform similarly well on the Sentinel-1 data. Due to the fact that the distribution of buoys and grid data is very sparse, with only around one and five vectors per image pair, respectively, the evaluations cannot statistically capture potential diversity in the entire image area. Fig. 6 provides

30

an indicative example of the calculated vectors on an image pair on the first of the selected areas (area S1, see Supplementary Material, enclosed within region SEN2 in Fig. 1). As observed, the vectors calculated from both optical flow and MCC in all image resolution versions are similar and well aligned with buoy and grid data. Only one buoy and four grid vectors fit inside this area, so a large part of the image is not adequately sampled. For instance, some inconsistent vectors are generated from optical flow and MCC on the bottom-left and the bottom-right parts of the image, respectively. A buoy or grid vector in the position of one such inconsistent vector may influence the statistical evaluation in favor of the optical flow or MCC and may favor one or the other in the overall statistics. However, in general, both methods provide similarly high quality vectors in all super-resolved versions. As an indicative example, MCC vectors on X8 images are the second most accurate compared with the NSIDC grid vectors. This further demonstrates that the accuracy of the vectors remains high even by upscaling images to 20 m spatial resolution, i.e., eight times finer than the original ones, or even outperforms results with coarser images.

As mentioned in Section 3.3, due to computational constraints and lack of density buoy vectors for validation, the originally acquired SAR images of 40 m spatial resolution are first downsampled to 160 m before our SR approach is applied. Thus, the X4 super-resolved images have the same resolution with the originally acquired SAR images. As a further evaluation step of our approach, we additionally calculate motion using the original SAR images. Table 6 presents the evaluation results. Comparing with Table 5, it is observed that the motion calculated by the original 40 m images falls

31
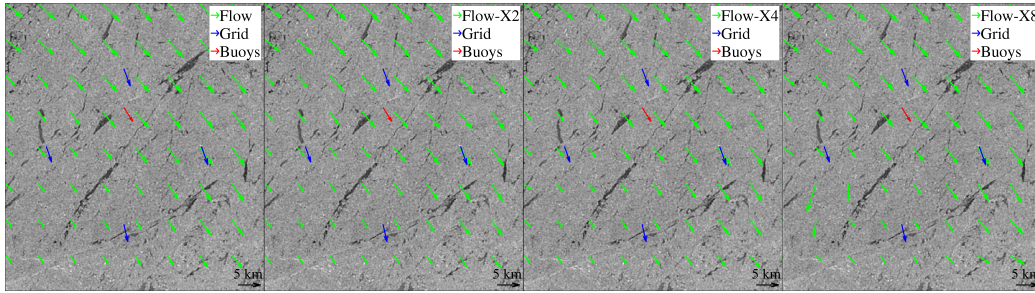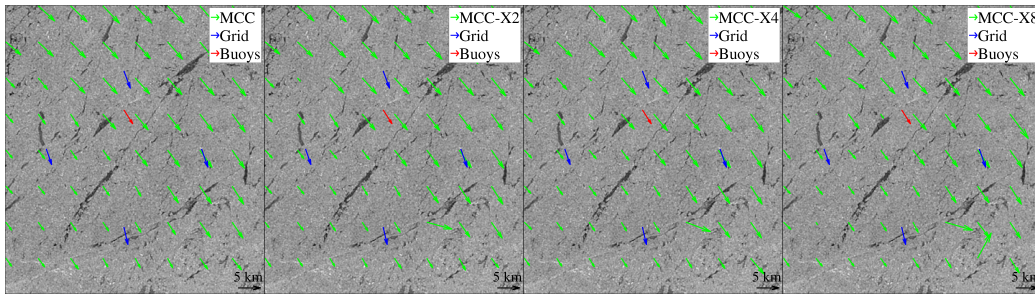
Figure 6: Calculated motion vectors on the original and super-resolved Sentinel-1 images for the first of the nine areas from Jan. 3 to Jan. 6, 2015. For better illustration, only subset of the vectors are drawn. (a) From left to right, optical flow vectors from the original and super-resolved images by a factor of two, four, and eight. (b) The respective MCC vectors.

between the results obtained with the X2 and X4 super-resolved images. The original image results are similar with the optical flow X4 results for the x axis, whereas outperforming the latter for MCC and the optical flow on the y axis. The results are promising for the performance of the proposed SR approach. It is also noteworthy that the motion calculation on the 80 m X2 super-resolved images is more accurate than the original SAR images, whose spatial resolution is doubled. This is an indication of the ability of the proposed SR approach to maintain the structure of the original images

32

Table 6: Accuracy evaluation of the optical flow and MCC vectors, for the 40 m resolution 66 image pairs of the originally acquired Sentinel-1 images, against IABP buoys, 75 vectors for the overall period.

	δx				δy			
	MAE	RMSE	RSE	P	MAE	RMSE	RSE	P
Flow-orig	0.352	0.620	0.054	0.974	0.442	1.129	0.145	0.928
MCC-orig	0.317	0.504	0.036	0.983	0.409	0.686	0.054	0.984

and their sharpness to the degree appropriate for the detection of edges and shapes required for the accurate calculation of motion between image pairs.

6. Discussions

The experimental results demonstrate that the proposed combination of optical flow and super-resolution provides better or comparable results with finer scale images of two, four, or even eight times than the original ones. Comparison with previous studies, although not always straightforward due to variations in the study area, sensors, or validation sources, can further support this outcome. Table 7 reports the accuracies by previous state-of-the-art methods with similar validation means to this study, together with indicative results from the proposed approach that demonstrate its efficiency. Employing similar 36.5 GHz horizontal polarization AMSR-E data with 12.5 km spatial resolution, Meier and Dai (2006) reported RMSE of 4.5–4.83 km for the two motion directions. Our proposed approach provides almost half error values applying optical flow, while achieving up to four times upscaling, and similar results when upscaling by eight times. The results outperform even genuinely higher resolution AMSR-E data (Girard-Ardhuin and Ezraty,

33

2012). Regarding optical data, the super-resolved MODIS images provide accuracies on par or higher than previously reported accuracies, while increasing the spatial resolution of the motion vector field up to 29 m. Highly accurate motion estimation has been achieved in some previous studies (Thomas et al., 2011; Karvonen, 2012) with SAR data. However, despite the high resolution original images, the resulting motion vector field resolution is in the order of several hundred meters. On the contrary, the proposed approach manages to provide comparable performance while increasing the resolution of the final vector field, and is able to provide accurate estimation in up to 20 m spatial resolution; to our knowledge, this is the highest resolution reported in sea ice motion studies with satellite imagery.

As shown in the experimental results, optical flow outperforms the pattern matching method in most cases. However, in certain images, mainly at the highest super-resolved levels, MCC appears to provide more accurate motion vectors. This is mainly attributed to two reasons: i) In some images with texture with repetitive patterns or edges sharpened during super-resolution, the sparse correspondences detected in the second step of the optical flow calculation are not spatially consistent. These mis-calculated correspondences are then fed to the sparse-to-dense interpolation step, providing a weaker initialization input for the dense optical flow calculation. ii) Splitting large images into subimages, as necessary step due to memory limitation to calculate optical flow, provides weaker results than the ones where the entire process could run at once. This is explicitly tested by applying splitting into smaller images where direct processing is also feasible. In such cases, optical flow calculated on the entire image at one pass is more accurate than

34

Table 7: Comparison of the proposed approach with previous state-of-the-art studies, evaluated mainly with buoys. [a]Evaluated with 25-km NSIDC grid vectors. [b]Evaluated with sea ice beacons. [c]Spatial resolution of the final vector field is 400 m. [d]Spatial resolution of the final vector field is 800 m. [*]Error in vector magnitude.

Method	Data	Res.	MAE	RMSE
Passive microwave				
Meier and Dai (2006)	AMSR-E	12.5		4.50–4.83
Emery et al. (1997)	SSM/I	12.5		$\approx$6.00[*]
Girard-Ardhuin and Ezraty (2012)	AMSR-E	6.25		6.20–8.20[*]
Flow-X2	AMSR2	6.25	1.38–1.49	2.10–2.52
Flow-X4	AMSR2	3.125	1.28–1.72	2.00–3.20
Flow-X8	AMSR2	1.563	2.65–3.2	4.70–5.16
Optical				
Petrou and Tian (2017)	MODIS	0.232	2.88–4.72[a]	5.71–8.12[a]
Flow-X2	MODIS	0.116	1.15–1.28[a]	1.64–1.77[a]
Flow-X4	MODIS	0.058	1.55–1.81[a]	2.33–3.39[a]
Flow-X8	MODIS	0.029	1.58–3.04[a]	2.08–4.20[a]
SAR				
Komarov and Barber (2014)	RADARSAT-2	0.100		0.43[b*]
Thomas et al. (2011)	RADARSAT-1	0.050[c]	0.20–0.40	
Karvonen (2012)	RADARSAT-2, ASAR	0.1–0.15[d]	0.14–0.85[*]	
Flow-X2	Sentinel-1	0.080	0.36–0.44	0.60–1.05
MCC-X2	Sentinel-1	0.080	0.31–0.35	0.45–0.62
Flow-X8	Sentinel-1	0.020	0.65–0.73	1.75–2.04
MCC-X8	Sentinel-1	0.020	0.42–0.50	0.81–1.07

flow from merging the split images. This shortcoming is more evident in super-resolved images of a factor of eight, where splitting is more intense. Having adequate processing resources that would allow direct calculation in the entire image, the optical flow results are expected to be more accurate. It is noted that MCC is unaffected by this process, since no splitting is applied and all images are processed at one pass. Although our proposed SR methodology can be applied for an arbitrarily large upscaling factor, we limit upscaling to eight times in this study due to the memory constraints.

Application of super-resolution increases the density of the motion vector field by several times, i.e., 4, 16, and 64 times for the X2, X4, and X8 upscaling, respectively. This increase applies equally to both optical flow and MCC methods and is a main benefit of the proposed super-resolution component over previous approaches where upsampling was attempted implicitly on the resulting motion vector field. However, a further improvement brought by the optical flow is on the minimum detectable motion. As expected, MCC is able to capture one-pixel motion as the minimum non-zero motion. Although this improves as the resolution of the images increases, it is still coarser than the subpixel motion estimated by optical flow in the continuous space. It is also noteworthy that the calculation of optical flow is in general faster than MCC, especially when no image splitting is conducted. As an indicative example, it takes around 79 sec to calculate optical flow on an image pair of $720{\times}720$ pixels using a four-core Intel$^{\circledR}$ Xeon$^{\circledR}$ CPU E5506 at 2.13 GHz, while the computing time for MCC is around 263 sec, i.e., almost four times slower.

As a final note on the theoretical strengths and limitations of the proposed

36

SR approach, it is reminded that the approach uses a number of natural images to learn dependency relations between high-/low-resolution exemplars, through small patch instances. The motivation behind this is that natural images hold certain priors and small image patches (after normalization) tend to repeat themselves. Based on this observation, generic image super-resolution methods, trained with natural images, are suitable for images captured by imaging systems, as opposed to synthetic images. This is also confirmed in this paper. In situations where the target images do not obey such priors, e.g., in synthetic images, microscopy images, etc., the current generic image super-resolution approach is not expected to be appropriate.

Overall, the proposed approach is able to generate accurate daily motion vectors at a spatial resolution of up to 1.5 km for the entire Arctic using AMSR2 data. This resolution largely benefits enhancing large-scale modeling of climate and ocean-atmosphere interactions. On the other side, vector estimations at a resolution of 20 m, as achieved with the Sentinel-1 data, open the floor to more accurate fine-scale monitoring of sea ice at the level of the size of a ship, and safer navigation and sea operations. In this study, because of processing limitations, the SAR data are first downsampled by four times, whereas the maximum upscaling attempted by the SR algorithm for all sensor images is eight. Without such limitations, the proposed approach can be effective in estimating motion at an even higher resolution.

7. Conclusion

In this study, we have proposed a super-resolution and optical flow approach to estimate sea ice motion at fine scales. The approach managed to

37

increase both the density of the calculated motion vector field and the minimum detected motion at subpixel levels. The effectiveness of the proposed method is evaluated on data from three different types of sensors and spatial resolutions, namely coarse-resolution passive microwave, medium-resolution optical, and high-resolution SAR data. The proposed approach achieves increase of up to eight times in image resolution without sacrificing or even with increasing the accuracy of the estimated vectors compared with the original data. Comparison with a state-of-the-art pattern matching approach demonstrates the advantages brought by optical flow. The results support the use of the approach for regional and local level applications and its potential for further improvements.

Acknowledgment

References

Ardila, J. P., Tolpekin, V. A., Bijker, W., Stein, A., 2011. Markov-random-field-based super-resolution mapping for identification of urban trees in VHR images. ISPRS J. Photogramm. 66, 762–775.

Berg, A., Axell, L., Eriksson, L. E. B., 2013. Comparison between SAR derived sea ice displacement and hindcasts by the operational ocean model HIROMB. In: IEEE Int. Geoscience and Remote Sensing Symp. pp. 3630–3633.

Berg, A., Eriksson, L. E. B., 2014. Investigation of a hybrid algorithm for sea ice drift measurements using Synthetic Aperture Radar images. IEEE Trans. Geosci. Remote Sens. 52 (8), 5023–5033.

De Silva, L. W. A., Yamaguchi, H., Ono, J., 2015. Ice–ocean coupled computations for sea-ice prediction to support ice navigation in Arctic sea routes. Polar Res. 34, 25008.

Dollár, P., Zitnick, C. L., 2015. Fast edge detection using structured forests. IEEE Trans. Pattern Anal. Mach. Intell. 37 (8), 1558–1570.

Dong, C., Loy, C. C., He, K., Tang, X., 2015. Image super-resolution using deep convolutional networks. IEEE Trans. Pattern Anal. Mach. Intell. 38 (2), 295–307.

Emery, W. J., Fowler, C., Maslanik, J. A., 1997. Satellite-derived maps of Arctic and Antarctic sea-ice motion: 1988 to 1994. Geophys. Res. Lett. 24 (8), 897–900.

Emery, W. J., Fowler, C. W., Hawkins, J., Preller, R. H., 1991. Fram Strait satellite image-derived ice motions. J. Geophys. Res. 96 (C3), 4751–4768.

Fleet, D., Weiss, Y., 2006. Optical flow estimation. In: Paragios, N., Chen, Y., Faugeras, O. (Eds.), Handbook of Mathematical Models in Computer Vision. Springer, New York, NY, Ch. 15, pp. 239–257.

Gao, J., Lythe, M. B., 1996. The maximum cross-correlation approach to detecting translational motions from sequential remote-sensing images. Comput. Geosci. 22 (5), 525–529.

Gettelman, A., Rood, R. B., 2016. Demystifying Climate Models: A Users Guide to Earth System Models. Springer Berlin Heidelberg, Ch. 6, pp. 87–108.

Girard-Ardhuin, F., Ezraty, R., 2012. Enhanced arctic sea ice drift estimation merging radiometer and scatterometer data. IEEE Trans. Geosci. Remote Sens. 50 (7), 2639–2648.

Gutiérrez, S., Long, D. G., 2003. Optical flow and scale-space theory applied to sea-ice motion estimation in Antarctica. In: IEEE Int. Geoscience and Remote Sensing Symp. Vol. 4. pp. 2805–2807.

Haarpaintner, J., 2006. Arctic-wide operational sea ice drift from enhanced-resolution QuikScat/SeaWinds scatterometry and its validation. IEEE Trans. Geosci. Remote Sens. 44 (1), 102–107.

Haas, C., 2017. Sea ice thickness distribution. In: Thomas, D. N. (Ed.), Sea Ice, 3rd Edition. John Wiley & Sons, Chichester, UK, Ch. 2, pp. 42–64.

Hagen, R. A., Peters, M. F., Liang, R. T., Ball, D. G., Brozena, J. M., 2014. Measuring Arctic sea ice motion in real time with photogrammetry. IEEE Geosci. Remote Sens. Lett. 11 (11), 1956–1960.

Hollands, T., Dierking, W., 2011. Performance of a multiscale correlation algorithm for the estimation of sea-ice drift from SAR images: Initial results. Ann. Glaciol. 52 (57), 311–317.

Huang, J., Singh, A., Ahuja, N., 2015. Single image super-resolution from transformed self-exemplars. In: CVPR.

Karvonen, J., 2012. Operational SAR-based sea ice drift monitoring over the Baltic Sea. Ocean Sci. 8 (4), 473–483.

Kim, J., Lee, J. K., Lee, K. M., 2016. Deeply-recursive convolutional network for image super-resolution. In: CVPR.

Kimura, N., Nishimura, A., Tanaka, Y., Yamaguchi, H., 2013. Influence of winter sea-ice motion on summer ice cover in the Arctic. Polar Res. 32, 20193.

Komarov, A. S., Barber, D. G., 2014. Sea ice motion tracking from sequential dual-polarization RADARSAT-2 images. IEEE Trans. Geosci. Remote Sens. 52 (1), 121–136.

Kræmer, T., Johnsen, H., Brekke, C., 2015. Emulating Sentinel-1 Doppler radial ice drift measurements using Envisat ASAR data. IEEE Trans. Geosci. Remote Sens. 53 (12), 6407–6418.

Kwok, R., Schweiger, D. A., Rothrock, D. A., Pang, S., Kottmeier, C., 1998. Sea ice motion from satellite passive microwave imagery assessed with ERS SAR and buoy motions. J. Geophys. Res. 103 (C4), 8191–8214.

Lavergne, T., Eastwood, S., Teffah, Z., Schyberg, H., Breivik, L. A., 2010. Sea ice motion from low-resolution satellite sensors: An alternative method and its validation in the Arctic. J. Geophys. Res. 115 (C10), C10032.

Lee, J.-S., Pottier, E., 2009. Polarimetric SAR Radar Imaging: From Basic to Applications. CRC Press, Boca Raton, FL.

Leppäranta, M., Sun, Y., Haapala, J., 1998. Comparisons of sea-ice velocity fields from ERS-1 SAR and a dynamic model. J. Glaciol. 44 (147), 248–262.

Li, X., Ling, F., Du, Y., Feng, Q., Zhang, Y., 2014. A spatial-temporal Hopfield neural network approach for super-resolution land cover mapping with multi-temporal different resolution remotely sensed images. ISPRS J. Photogramm. 93, 76–87.

Martin, D., Fowlkes, C., Tal, D., Malik, J., 2001. A Database of Human Segmented Natural Images and its Application to Evaluating Segmentation Algorithms and Measuring Ecological Statistics. In: ICCV.

Meier, W. N., 2017. Losing Arctic sea ice: observations of the recent decline and the long-term context. In: Thomas, D. N. (Ed.), Sea Ice, 3rd Edition. John Wiley & Sons, Chichester, UK, Ch. 11, pp. 290–303.

Meier, W. N., Dai, M., 2006. High-resolution sea-ice motions from AMSR-E imagery. Ann. Glaciol. 44, 352–356.

Meier, W. N., Maslanik, J. A., 2003. Effect of environmental conditions on observed, modeled, and assimilated sea ice motion errors. J. Geophys. Res. 108 (C5), 3152.

Meier, W. N., Maslanik, J. A., Fowler, C. W., 2000. Error analysis and assimilation of remotely sensed ice motion within an Arctic sea ice model. J. Geophys. Res. 105, 3339–3356.

Merino, M. T., Núñez, J., 2007. Super-resolution of remotely sensed images with variable-pixel linear reconstruction. IEEE Trans. Geosci. Remote Sens. 45 (5), 1446–1457.

Ninnis, R. M., Emery, W. J., Collins, M. J., 1986. Automated extraction of pack ice motion from advanced very high resolution radiometer imagery. J. Geophys. Res. 91 (C9), 10725–10734.

NSIDC, 2016. Documentation: Polar stereographic projection and grid. National Snow and Ice Data Center. [Online]. Available: http://nsidc.org/data/polar-stereo/ps_grids.html, Accessed on: Jul. 18, 2016.

Petrou, Z. I., Tian, Y., 2017. High-resolution sea ice motion estimation with optical flow using satellite spectroradiometer data. IEEE Trans. Geosci. Remote Sens. 55 (3), 1339–1350.

Rampal, P., Weiss, J., Marsan, D., 2009. Positive trend in the mean speed and deformation rate of Arctic sea ice, 1979–2007. J. Geophys. Res. 114 (C5), C05013.

Revaud, J., Weinzaepfel, P., Harchaoui, Z., Schmid, C., 2015. EpicFlow: Edge-preserving interpolation of correspondences for optical flow. In: IEEE Conf. Computer Vision and Pattern Recognition. pp. 1164–1172.

Russell, B. C., Torralba, A., Murphy, K. P., Freeman, W. T., 2008. LabelMe: A database and web-based tool for image annotation. Int. J. Comput. Vision 77, 157–173.

Small, D., Schubert, A., 2008. Guide to ASAR geocoding. Tech. Rep. 1.0, University of Zurich, ESRIN contract no. 20907/07/I-EC.

Smedsrud, L. H., Sirevaag, A., Kloster, K., Sorteberg, A., Sandven, S., 2011. Recent wind driven high sea ice area export in the Fram Strait contributes to Arctic sea ice decline. Cryosphere 5 (4), 821–829.

Spreen, G., Kwok, R., Menemenlis, D., 2011. Trends in arctic sea ice drift and role of wind forcing: 1992–2009. Geophys. Res. Lett. 38 (19), L19501.

Sun, Y., 1996. Automatic ice motion retrieval from ERS-1 SAR images using the optical flow method. Int. J. Remote Sens. 17 (11), 2059–2087.

Szeliski, R., 2011. Computer Vision: Algorithms and Applications. Springer, London, United Kingdom.

Thomas, M., Geiger, C. A., Kambhamettu, C., 2008. High resolution (400 m) motion characterization of sea ice using ERS-1 SAR imagery. Cold Reg. Sci. Technol. 52, 207–223.

Thomas, M., Kambhamettu, C., Geiger, C. A., 2011. Motion tracking of discontinuous sea ice. IEEE Trans. Geosci. Remote Sens. 49 (12), 5064–5079.

Tschudi, M., Fowler, C., Maslanik, J., Stewart, J. S., Meier, W., 2016a. Polar Pathfinder daily 25 km EASE-Grid sea ice motion vectors, version 3, Buoys. Boulder, Colorado USA: NASA National Snow and Ice Data Center Distributed Active Archive Center, doi: http://dx.doi.org/10.5067/O57VAIT2AYYY. Accessed: Dec. 20, 2016.

Tschudi, M., Fowler, C., Maslanik, J., Stewart, J. S., Meier, W., 2016b. Polar Pathfinder daily 25 km EASE-Grid sea ice motion vectors, version 3, Daily Grids. Boulder, Colorado USA: NASA National Snow and Ice Data Center Distributed Active Archive Center, doi: http://dx.doi.org/10.5067/O57VAIT2AYYY. Accessed on: Jul. 14, 2016.

Tschudi, M., Fowler, C., Maslanik, J., Stroeve, J., 2010. Tracking the movement and changing surface characteristics of Arctic sea ice. IEEE J. Sel. Topics Appl. Earth Observ. Remote Sens. 3 (4), 536–540.

Vermote, E., Wolfe, R., 2015. MOD09GQ MODIS/Terra surface reflectance daily L2G global 250m SIN grid v006. NASA EOSDIS Land Processes DAAC, 2015. Doi: http://doi.org/10.5067/MODIS/MOD09GQ.006.

Weinzaepfel, P., Revaud, J., Harchaoui, Z., Schmid, C., 2013. DeepFlow: Large displacement optical flow with deep matching. In: IEEE Int. Conf. Computer Vision. pp. 1385–1392.

Xian, Y., Petrou, Z. I., Tian, Y., Meier, W. N., 2017. Super-resolved fine scale sea ice motion tracking. IEEE Trans. Geosci. Remote Sens.In print.

Xian, Y., Tian, Y., 2016. Single image super-resolution via internal gradient similarity. J. Vis. Commun. Image R. 35, 91–102.

Xian, Y., Yang, X., Tian, Y., 2015. Hybrid example-based single image super-resolution. In: ISVC.

Yang, J., Lin, Z., Cohen, S., 2013. Fast image super-resolution based on in-place example regression. In: CVPR.